BIOCHEMISTRY
including biophysical chemistry & molecular biology

Article

pubs.acs.org/biochemistry

Empirical Valence Bond Simulations of the Chemical Mechanism of ATP to cAMP Conversion by Anthrax Edema Factor

Letif Mones,[†] Wei-Jen Tang,[‡] and Jan Florián*[,†]

[†]Department of Chemistry, Loyola University Chicago, Chicago, Illinois 60660, United States

[‡]Ben May Department for Cancer Research, The University of Chicago, Chicago, Illinois 60637, United States

Supporting Information

ABSTRACT: The two-metal catalysis by the adenylyl cyclase domain of the anthrax edema factor toxin was simulated using the empirical valence bond (EVB) quantum mechanical/molecular mechanical approach. These calculations considered the energetics of the nucleophile deprotonation and the formation of a new P−O bond in aqueous solution and in the enzyme−substrate complex present in the crystal structure models of the reactant and product states of the reaction. Our calculations support a reaction pathway that involves metal-assisted transfer of a proton from the nucleophile to the bulk aqueous solution followed by subsequent formation of an unstable pentavalent intermediate that decomposes into cAMP and pyrophosphate (PP_i). This pathway involves ligand exchange in the first solvation sphere of the catalytic metal. At 12.9 kcal/mol, the barrier for the last step of the reaction, the cleavage of the P−O bond to PP_i, corresponds to the highest point on the free energy profile for this reaction pathway. However, this energy is too close to the value of 11.4 kcal/mol calculated for the barrier of the nucleophilic attack step to reach a definitive conclusion about the rate-limiting step. The calculated reaction mechanism is supported by reasonable agreement between the experimental and calculated catalytic rate constant decrease caused by the mutation of the active site lysine 346 to arginine.

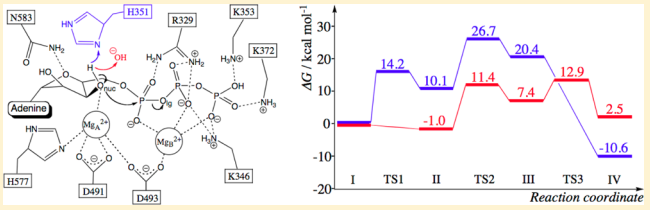

Cyclic AMP (cAMP) is a key second messenger in cellular responses to extracellular stimuli such as hormones and neurotransmitters. The elevation of the intracellular cAMP level modulates a diverse set of physiological responses, including carbohydrate and lipid metabolism, cell differentiation, apoptosis, neuronal activities, and ion homeostasis.[1−3] Many infectious organisms secrete virulence factors that increase cAMP levels within infected host cells, thus disrupting intracellular signaling pathways. One mechanism is to secrete toxins with adenylyl cyclase activity that enter host cells and increase the level of intracellular cAMP. Two better-studied adenylyl cyclase toxins are edema factor (EF) secreted by anthrax bacterium *Bacillus anthracis*[4,5] and CyaA secreted by *Bacillus pertussis*, the causative agent of pertussis (or whooping cough).[6] EF enters into host cells by anthrax protective antigen-assisted translocation.[7] EF can profoundly retard immune surveillance, particularly on macrophages, dendritic cells, and T cells, alter functions of endothelial cells, and lead to dysfunction of the cardiovascular system.[5,8] Consistent with this notion, the defect in the EF gene leads to reduced virulence of anthrax bacteria, and an approved drug that blocks the activity of EF can reduce anthrax-caused mortality in mice.[5,9]

EF consists of two functional domains (Figure 1). The N-terminal domain is an anthrax protective antigen-binding domain, which facilitates the entrance of EF into the intracellular space. The C-terminal domain is a calmodulin (CaM)-activated adenylyl cyclase domain (ACD). EF adenylyl cyclase belongs to the adenylyl cyclase toxin family (class II). Despite catalyzing the same reaction, this toxin family has no structural homology with the mammalian adenylyl cyclases.[10,11] The first crystallographic study of the EF-ACD−CaM−3′-dATP complex [Protein Data Bank (PDB) entry 1K90][11] showed the presence of one metal ion coordinated to both α- and β-phosphates of dATP, as opposed to two-metal catalysis implied by the structure of mammalian adenylyl cyclase.[10,12] The two-metal ion catalysis, which is a prevalent mechanism in DNA polymerases and some endonucleases,[13−15] is used by mammalian adenylyl cyclase to facilitate formation of cAMP from ATP. The role of the second metal in facilitating the deprotonation of the 3′-OH group of ATP seemed to be performed in EF-ACD by histidine 351, resulting in a catalytic efficiency, k_{cat}/K_M, of EF-ACD more than 2 orders of magnitude larger than that of mammalian cyclase.[16] Such a high level of production of cAMP, a second cellular messenger, overwhelms the cell signaling pathways leading to its death. Thus, a detailed knowledge of the EF-ACD catalytic mechanism is important for preventing and defending against anthrax outbreaks.

The case for a single-metal general base catalytic mechanism was weakened by the site-directed mutagenesis of His 351 to lysine, which had almost no effect on k_{cat}.[17] The role of the general base could be substituted by the second metal ion. This

Received: January 23, 2013
Revised: March 11, 2013
Published: March 12, 2013

dx.doi.org/10.1021/bi400088y | *Biochemistry* 2013, 52, 2672−2682

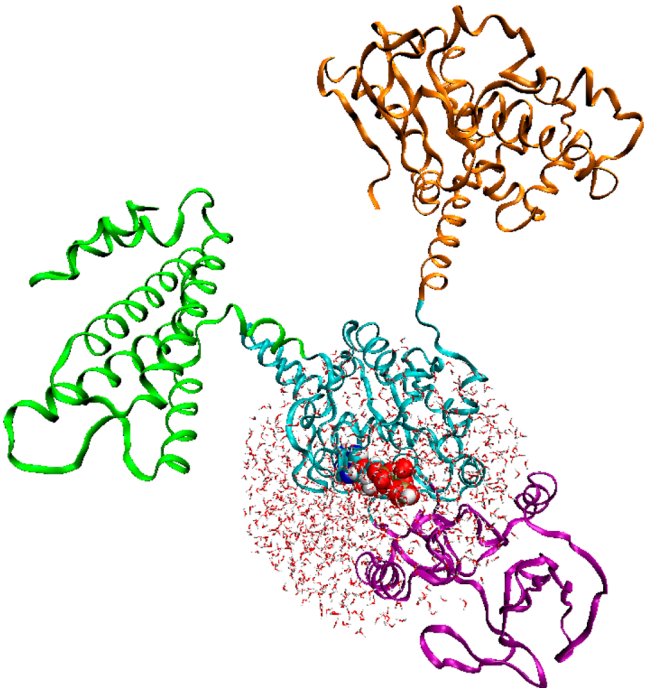

Figure 1. Edema factor toxin (orange, protective antigen-binding domain; cyan, C_A catalytic core; purple, C_B catalytic core; green, helical domain of the adenylyl cyclase domain, ACD) in cartoon representation. The simulated part of the enzyme and the ATP substrate are enclosed in a droplet of water molecules.

ion was observed in a more recent X-ray structure of the EF–CaM–3′-dATP complex (PDB entry 1XFV).[17] However, this crystal structure had a lower resolution of 3.35 Å. Thus, one or both of the reported Mg^{2+} ions could actually represent Na^+ or a water molecule. Molecular dynamics simulations of ATP binding based on the 1XVF structure[17] indicated that His 351 is unlikely to directly function as a general base but could still play a role in assisting a water molecule or OH^- ion to deprotonate the 3′-OH of ATP. Interestingly, the structure of EF-CaM that was cocrystallized with cAMP and pyrophosphate (PDB entry 1SK6)[16] (i.e., with the reaction products) also showed two metal ions in the active site. However, Mg^{2+} ions were replaced by Yb^{3+} ions in this structure, and a partial occupancy of double- and single-ion configurations was needed to reproduce the observed electron density.

The one-metal reactant (PDB entry 1K90) and product (PDB entry 1SK6) structures contain substrates and products in orientations that are similar enough[18] to be consistent with expected concerted or nearly concerted P–O bond forming and breaking processes during the catalytic reaction.[17] The largest conformational difference between these structures resides in the adenine moiety that is in the anti orientation in the structure with bound dATP but in the syn orientation in the product structure. In contrast, the two-metal reactant (PDB entry 1XFV) and product structures do not appear to be two snapshots along the same mechanistic pathway. This is because, in addition to the difference in the torsional angle of the glycosidic bond, there is a large difference in the conformation and orientation of their triphosphate–PP_i moieties.[17,18]

In this study, we investigate the energetics of two-metal ion catalysis (Figure 2) of the wild-type (WT) EF-ACD and its K346R mutant using quantum mechanical/molecular mechanical (QM/MM) computer simulations. We calculated free

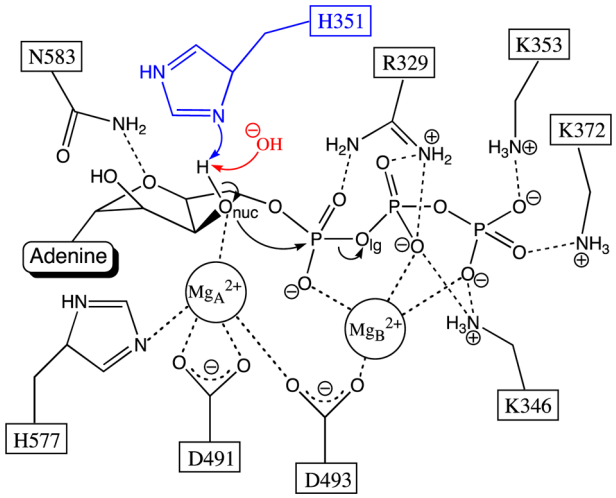

Figure 2. Schematic topology of the active site of EF-ACD with a bound ATP substrate. The associative mechanism is denoted by arrows. The initial proton transfer from the 3′-OH nucleophile (O_{nuc}) to His 351 (general base, GB, mechanism) is indicated by the blue arrow. An alternative extrinsic (EX) mechanism for the abstraction of a proton from O_{nuc} may involve OH^- (colored red) that diffuses into the active site from the aqueous solution.

energy profiles for the conversion of ATP to cAMP and pyrophosphate (PP_i) while considering two different conformations of the substrate and two possible mechanistic options for the deprotonation of the 3′-O nucleophile. First, we examined a direct proton transfer from the 3′-OH group of ribose to His 351 (general base mechanism), followed by the nucleophilic attack and PP_i departure steps. Alternatively, we evaluated the ATP cyclization initiated by the ribose that is already in its deprotonated state in equilibrium (extrinsic mechanism) while also taking into account the free energy cost of forming such a deprotonated nucleophile at pH 7. In this calculation, we assumed that the protonated and deprotonated states of the nucleophile are in a fast equilibrium determined by its calculated pK_a in the protein and the pH of the aqueous solution. To examine the role of substrate conformation, each reaction mechanism was independently simulated using initial structures of the EF-ACD–ATP complex generated from the 1XFV and 1SK6 crystal structures.

All reaction surfaces were generated using the empirical valence bond (EVB) method.[19,20] In a conventional implementation of this approach, the classical molecular dynamics (MD) simulations are first driven from the "reactant" to the "product" state of a single-step reaction using a coupling parameter λ. The EVB energies are then calculated for geometries sampled by MD simulations, and the EVB-based free energies are plotted along a collective "E_{gap}" reaction coordinate using the umbrella sampling approach.[19,21] In this study, we improved the sampled energy space by "pooling" MD and EVB energies obtained from independent simulations of the reaction in the forward ($\lambda = 0 \rightarrow \lambda = 1$) and reverse ($\lambda = 1 \rightarrow \lambda = 0$) directions. The free energy surfaces calculated using the pooled EVB approach showed improved stability and agreement with the observed rate constants.

METHODS

Calculations of the Free Energy Profiles. To compute the total free energy differences and activation barriers of the different reaction steps, the EVB theory[19,20] was applied in

dx.doi.org/10.1021/bi400088y | Biochemistry 2013, 52, 2672–2682

combination with the free energy perturbation (FEP) technique and MD simulations. In the EVB method, the reaction free energy profile is calculated on the ground state energy surface, E_g. E_g equals the lowest eigenvalue of the EVB Hamiltonian, H, for the studied system. The diagonal elements of matrix **H** are represented by classical potential energy functions of the diabatic valence bond states (i.e., reactant and product states for the two-state EVB) of the investigated elementary reaction step:

$$H_{ii} = \varepsilon_i = \sum_{q=1}^{N_q} D_q^i\{1 - \exp[-a_q^i(b_q - b_{q,0}^i)]\}^2 + \frac{1}{2}\sum_{j=1}^{N_b} k_{j,b}^i(r_j - r_{j,0}^i)^2 + \frac{1}{2}\sum_{l=1}^{N_a} k_{l,a}^i(\theta_l - \theta_{l,0}^i)^2 + \sum_{m}^{N_t} k_{m,t}^i[1 + \cos(n_m^i\phi_m^i - \delta_m^i)] + \sum_{p,s=1}^{N_{nb}} U_{nb,ps}^i + \alpha^i \quad (1)$$

where the first term represents a Morse potential of the qth affected (breaking or forming) bond in the ith state, the second term is the harmonic potential for the other bonds, the third and fourth terms are the angle and torsion potentials for the covalently bonded atoms, respectively, and $U_{nb,ps}^i$ is the nonbonded interaction energy, including the electrostatic and van der Waals contributions. α^i is the gas phase energy of the ith state when the reacting fragments are separated to the infinity. The off-diagonal elements are usually represented by simple-exponential functions

$$H_{ij} = A_{ij}\exp[-\mu_{ij}(r_{ab} - r_{ab,0})] \quad (2)$$

or, as in this work, by constant functions that are activated in the program input by setting μ_{ij} equal to zero. In eq 2, r_{ab} represents the distance between two atoms characterizing the affected bond between the ith and jth states, and A_{ij}, μ_{ij}, and $r_{ab,0}$ are empirical constants. The values of α^i, A_{ij}, and μ_{ij} are calibrated on the basis of the computational reproduction of the experimental free energy profile (or high-level ab initio data) for the reference reaction in aqueous solution that has the same mechanism as the reaction in the enzyme. In the conventional EVB approach (discussed below), the system is driven on a parameter-free potential. Because the values of α^i, A_{ij}, and μ_{ij} are absent from these forces, their parametrization is conveniently performed after completion of MD simulations.

To simulate the formation of the chemical bond during the transition between two EVB states, ε_1 and ε_2 (initial and final states, respectively), we conduct MD simulations of the system on an artificial potential (mapping potential, ε_m) that is determined by a linear combination of the initial and final states:

$$\varepsilon_m(\lambda_k) = (1 - \lambda_k)\varepsilon_1 + \lambda_k\varepsilon_2 \quad (3)$$

where λ_k is an order parameter going from 0 to 1 in $N + 1$ windows (so k takes integer values from 0 to N) as the initial state is changed to the final state. The free energy change between the consecutive steps can be calculated by Zwanzig's formula[21]

$$\Delta G_{k\to k+1} = -\beta^{-1}\ln\langle\exp\{-\beta[\varepsilon_m(\lambda_{k+1}) - \varepsilon_m(\lambda_k)]\}\rangle_k \quad (4)$$

where the broken brackets mean an averaging over the trajectory performed on the kth mapping potential and $\beta = 1/(k_BT)$, where k_B is Boltzmann's constant and T is the temperature in kelvin. The total free energy between the two states is the sum of $\Delta G_{k\to k+1}$ perturbations:

$$\Delta G(\varepsilon_1 \to \varepsilon_2) = \sum_{k=0}^{N-1}\Delta G_{k\to k+1} \quad (5)$$

After the completion of MD-FEP calculations, we computed the entire free energy profile (and determined the activation barrier) using the umbrella sampling (US) method. This method determines the potential of mean force, Δg, on the ground state EVB energy surface (E_g) using eq 6:

$$\Delta g(X) = \left\langle \sum_{k=0}^{i-1}\Delta G_{k\to k+1} - \frac{1}{\beta}\ln\langle\delta(X - X')\exp\{-\beta[E_g - \varepsilon_m(\lambda_i)]\}\rangle_{\varepsilon_m}\right\rangle_i \quad (6)$$

where the first term on the right-hand side represents the free energy difference between the first and ith mapping potentials (MD-FEP, eq 5), δ denotes Dirac's delta function, and the inner broken brackets ($\langle\ldots\rangle_{\varepsilon_m}$) denote the average over the trajectory performed on the given (ith) mapping potential (eq 3). The outer broken brackets ($\langle\ldots\rangle_i$) symbolize an average over contributions from all mapping potentials to the free energy profile. Our general coordinate was evaluated (after the completion of MD simulations) as the energy difference between the energies of the initial and final diabatic states

$$X = E_{gap} = \varepsilon_1 - \varepsilon_2 \quad (7)$$

Using eq 7, a reaction coordinate value was assigned to all configurations of the reacting system that were sampled during our MD simulations. This reaction coordinate is usually subdivided into M equidistant bins. The resolution provided by this discretization is practically limited by the need for each bin to include statistically significant numbers of sampled geometries. Equations 6 and 7 allow us to calibrate the EVB parameters and reproduce the free energy profile of the reference reaction after the completion of MD simulations.

Models of the Reacting System in the Enzyme. Models based on the "reactant" structure were derived from the crystal structure of EF-CaM with dATP (PDB entry 1XFV[17]). Models based on the "product" structure were generated from the EF-CaM−cAMP−PP_i complex (PDB entry 1SK6[16]). In the latter case, the crystallographic structure contained ytterbium ions, which were replaced with catalytically active magnesium ions, so all enzymatic models contained two magnesium ions in the catalytic center. Protein residues were completed with hydrogen atoms using the Amber 9 program package.[22] Furthermore, crystallographic water molecules and CaM were removed, and the crystal structures have been immersed in a sphere of TIP3P water molecules with a 24 Å radius centered on the P_α atom of ATP or cAMP. The positions of ACD atoms that protruded outside this 24 Å simulation sphere (Figure 1) were constrained at their coordinates observed in the crystal structure.

The 3′-OH group was manually added to dATP; the resulting ATP and PP_i were protonated at the O2γ atom (Figure 1S of the Supporting Information), resulting in a total

dx.doi.org/10.1021/bi400088y | Biochemistry 2013, 52, 2672−2682

charge of −3 au for ATP and PP_i. The use of the triphosphate moiety that carries a charge of −3 au deviates from the charge of −4 au employed in our earlier computational studies.[14,17,23−25] This methodological change was introduced to improve the agreement between the calculated and experimental geometries of the arginine 149 residue in the active site of DNA polymerase β by reducing overestimated electrostatic interactions between arginine 149 and the nearby γ-phosphate.[26] This approach was retained in this study because we believe that reducing the high charge of γ-phosphate increases the reliability of the computer simulations that do not examine chemical transformations of this group.

The total charge of the Glu, Asp, Lys, and Arg residues was set to be consistent with their pK_a constants in water; residues more than 18 Å from the P_α atom of ATP or cAMP were kept in their electroneutral form. All His residues were kept in their neutral N_δ-H form. These protonation settings ensured overall electroneutrality of each simulation sphere that was used to simulate the reaction mechanism involving the transfer of a proton to the general base. Therefore, no counterions were added to the simulated system. An additional glutamate acid residue (Glu 381) was protonated during simulations of the mechanism involving the transfer of a proton to the bulk water (extrinsic mechanism), so that the overall neutrality of the simulated system could be established after the annihilation of the proton on the nucleophile. The initial structure of the mutant protein was generated from the reactant crystal structure by manually changing side chain atoms of lysine 346 to arginine.

Models of the Reacting System in Water. Models used to investigate the reference reaction for the general base mechanism in water included a protonated ATP (or cAMP and PP_i for the product structure), a capped histidine residue, two magnesium ions, and one chloride ion to achieve overall electroneutrality. Three models were used to investigate the extrinsic mechanism: two of them included an adenosine, a capped histidine residue, and a sodium ion (at different positions), while the third one contained a protonated ATP, a capped histidine residue, and two magnesium ions. The third model was used also for calculations of the two reaction steps that followed the initial deprotonation of the nucleophile. Each model was filled with a 24 Å radius water droplet centered on the O3′ atom.

MD Simulations. MD calculations were conducted using the Amber 94 force field[27] implemented in Q version 5.06.[28] Nonstandard force field parameters for magnesium ion,[14] protonated ATP, adenosine, cAMP, protonated PP_i, and the pentavalent phosphorane intermediate are described in the Supporting Information (Tables 5S−16S).

Production MD trajectories were obtained using a 1.0 fs integration step. The SHAKE algorithm[29] was applied to all hydrogen atoms outside the reacting region. All nonbonded interactions of the reacting part were considered explicitly, while the remaining nonbonded interactions were evaluated using a combination of a 10 Å cutoff radius and the local reaction field (LRF) approximation[30] for the long-range electrostatic interactions reaching beyond this cutoff. For the outer water shell, which included water molecules within 3 Å of the edge of the simulation sphere, a polarization restraint was applied (with a 20 kcal mol^{-1} rad^{-2} force constant).

The initial relaxation of each protein structure was performed using the following protocol. First, the system was gradually heated from 1 to 300 K in a 200 ps simulation, while a 50 kcal mol^{-1} $Å^{-2}$ harmonic force constant was applied on the solute atoms to restrain them to their positions in the crystal structure. This procedure resulted in the equilibration of the solvent around the solute molecule. During an additional 185 ps, the system was gradually cooled to 5 K using the same harmonic force constant to restrain positions of the solute atoms. The restraining force constants were gradually decreased to 1 kcal mol^{-1} $Å^{-2}$ in a subsequent 30 ps simulation at 5 K. Finally, the system was gradually reheated to 300 K during a 150 ps simulation, and an additional 100 ps equilibration was applied at 300 K (using a 1 kcal mol^{-1} $Å^{-2}$ force constant on the solute atoms; these restraints were removed in production FEP calculations).

The reference systems in aqueous solution were equilibrated by being gradually heated from 1 to 300 K in a 150 ps simulation. At 300 K, an additional 100 ps simulation was conducted to further relax the simulated system. Calculations of each reaction step included a 1 ns FEP MD simulation that was subdivided into 51 windows. In aqueous solution, only a 1 kcal mol^{-1} $Å^{-2}$ positional restraint was applied to keep the center of mass of the solute in the center of the water droplet.

Additional distance restraints were applied depending on the investigated reaction step in aqueous solution or enzymatic environment. In the reactions involving the transfer of a proton to the general base, the distance between the proton donor and acceptor atoms was restrained using a flat-bottom harmonic potential, which was characterized by a 10 kcal mol^{-1} $Å^{-2}$ harmonic force constant applied for distances of <1.0 and >3.0 Å. For the P−O bond formation and cleavage reaction steps, a similar restraint was used between the phosphorus and the attacking or leaving oxygen atom. In this case, the flat region of the potential was located between 1.0 and 4.4 Å.

EVB Calculations. The reactive (QM) region that was used in EVB calculations included 26 atoms belonging to the α- and β-phosphate groups, the imidazole moiety of His 351, and a part of the ATP sugar (Figure 3 and Figure 1S of the Supporting Information). This EVB QM region was used in all calculations in water or protein when ATP or cAMP with PP_i was present. For the reference reaction in water involving adenosine in place of ATP, the EVB QM region included imidazole protonated on the N_δ atom, and a $HO_{5'}$−$HC_{5'}H$−$C_{4'}H$−$C_{3'}H$−$O_{3'}H$ ribose fragment (total of 19 atoms).

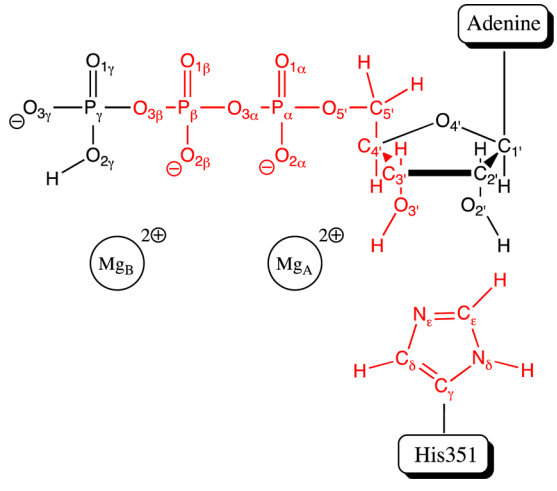

Figure 3. Definition of the QM EVB region (red) of the simulated systems.

dx.doi.org/10.1021/bi400088y | *Biochemistry* 2013, 52, 2672−2682

Definition of Valence Bond States. We considered two alternative proton transfer pathways (extrinsic, e, and general base, g) to deprotonate the O3′ nucleophile. Both protonation pathways were evaluated in the context of the forward reaction (ATP → cAMP + PP_i) in the WT and mutant enzymes and the backward reaction (cAMP + PP_i → ATP) in the WT. Eleven valence bond states (resonance structures) that were used in the EVB calculations of individual reaction steps are presented in Figure 4. These states include a reactant state for the forward reaction, Ie/fw (or equivalently Ig/fw), and the product state of the backward reaction, Ie/bw (or equivalently Ig/bw). Note that the Ie/bw state differs from the Ie/fw state in the protonation state of His 351. Our adoption of this structural difference was motivated by differences in the crystallographic position of His 351 that are present in the structures of PDB entries 1XVF and 1SK6. The studied valence bond states also include the deprotonated intermediates with a negatively charged O3′ nucleophile for the general base, IIg, and extrinsic, IIe, mechanisms, the pentavalent phosphorane intermediates, IIIe and IIIg, the product states of the forward reaction, IVe/fw and IVg, and the reactant states of the backward reaction, IVe/bw and IVg.

Pooled Sampling. To increase the efficiency of sampling in EVB simulations, we introduced a new technique termed pooled sampling (PS). The main idea is to calculate a single free energy profile of a given reaction step based on the configurations sampled in both the forward and reverse FEP simulations. Instead of calculating a simple average free energy profile from the forward and reverse profiles, we pooled the sampled points with the appropriate λ values together. The construction of mapping potentials is similar for the forward and reverse reactions (eq 3), the only difference being the direction of their change. In the forward FEP simulation, λ_k changes from 0 to 1 as k increases from 0 to N, whereas in the reverse simulation, λ_k changes from 1 to 0 as k increases from 0 to N. Therefore, to collect the energy points (ε_m) that belong to the same mapping potential, we have combined the forward and reverse energies as follows:

$$\{\varepsilon_m^{\text{pooled}}(\lambda_k)\} = \{\varepsilon_m^{\text{fw}}(\lambda_k)\} \cup \{\varepsilon_m^{\text{rev}}(1-\lambda_k)\} \quad (8)$$

With these merged sets of mapping potentials, we can apply the standard EVB–US process (eq 6) for the pooled points as if they were from a single (one-direction) FEP simulation.

RESULTS

Energetics of the Reference Reaction in Aqueous Solution. The overall reaction and activation free energies for the studied reaction in aqueous solution have not been measured because the hydrolysis of ATP in aqueous solution occurs preferentially on the γ-phosphorus, yielding ADP and inorganic phosphate, P_i. For the ease of calibration of our EVB model, the ATP → cAMP + PP_i reaction was split into three separate two-state reaction steps: the nucleophile generation (proton transfer, PT), the nucleophilic attack (NA), and the departure of the leaving group (DL). A combination of experimental kinetics and thermodynamics and ab initio quantum chemical data were used to determine the energetics of these steps in aqueous solution.

PT Reactions in Aqueous Solution. Reaction free energies for proton transfer (PT) reactions were determined using the difference in the experimental pK_a of the proton donor and the conjugate acid of its acceptor

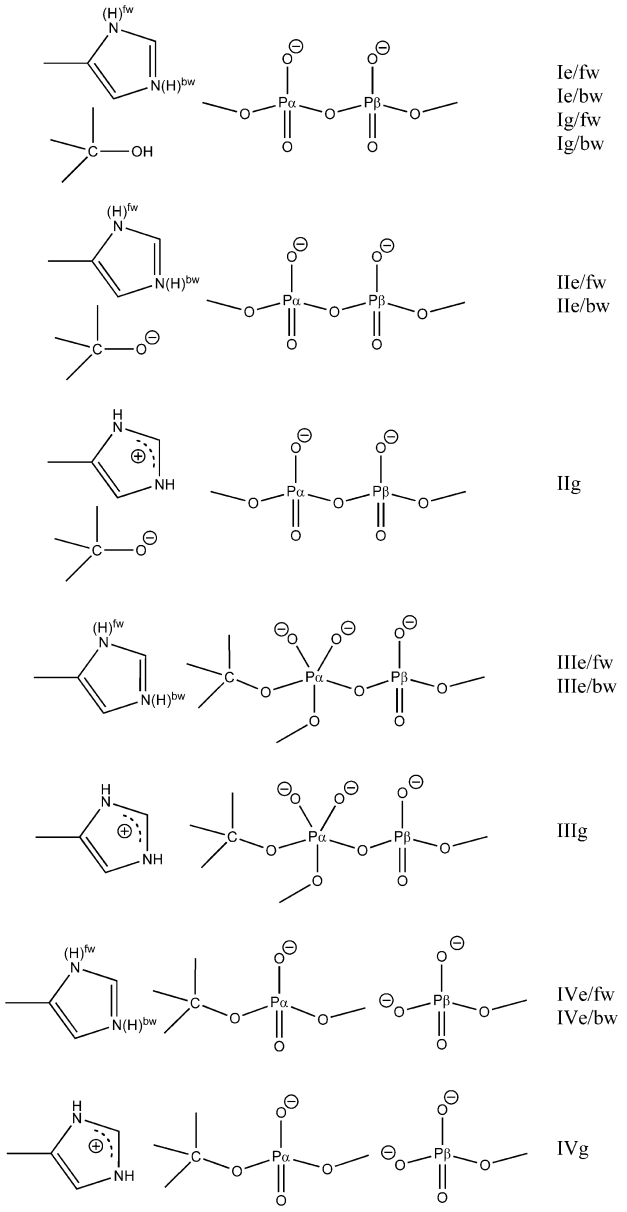

Figure 4. Valence bond states that were used in our EVB calculations. Each state is denoted in the text using a combination of a Roman numeral and g and e, fw, and bw abbreviations that provide information about mechanistic and computational pathways, in which this state plays a role. The phrases "forward reaction" and "backward reaction" refer to the overall ATP → cAMP + PP_i and cAMP + PP_i → ATP reactions, respectively, whereas the "reverse reaction" or "reverse direction" denotes a single reaction step that was driven by the FEP mapping from a valence bond state labeled in this figure with a higher Roman numeral to a state labeled by a lower Roman numeral: I, His with ATP (note that this is the reactant state of the forward reaction as well as the product state of the backward reaction); II, deprotonated intermediate state; III, pentavalent intermediate state; IV, His + PP_i + cAMP, i.e., the product state of the forward reactions and the reactant state of the backward reaction. e denotes the extrinsic mechanism. g denotes the general base mechanism (in this mechanism, His becomes doubly protonated from state II). fw denotes the forward reaction with the imidazole ring protonated on N_δ. bw denotes the backward reaction with the imidazole ring protonated on N_ε. Note that for IIg, IIIg, and IVg states, the forward and backward resonance states are identical because the histidine is doubly protonated.

dx.doi.org/10.1021/bi400088y | *Biochemistry* 2013, 52, 2672–2682

$$\Delta G_{PT} = 2.303RT[pK_a(\text{donor}) - pK_a(\text{acceptor})] \quad (9)$$

where R and T denote the universal gas constant and the thermodynamic temperature, respectively. For the general base mechanism with histidine (pK_a = 6.1) being the proton acceptor and adenosine (pK_a = 12.35[31]) the donor (Figure 2), ΔG_{PT} = 8.6 kcal mol^{-1}. A small activation barrier for this reaction was assumed because the PT reactions between N and O atoms with similar pK_a values are very fast in solution,[32] thus yielding the overall forward activation free energy of 10 kcal mol^{-1}. The free energy for nucleophile deprotonation by the extrinsic mechanism at pH 7 was calibrated as 7.3 kcal mol^{-1} using the strategy described in refs 14 and 15.

cAMP Formation in Aqueous Solution. The observed standard reaction free energy for the ATP → cAMP + PP_i reaction is 1.6 kcal mol^{-1}.[33] Because the products stay in contact in our simulations of the reaction in aqueous solution, we added to this free energy an estimated entropic penalty of 2.4 kcal mol^{-1} [=RT ln(55.56)] to arrive to the reaction free energy of 4.0 kcal mol^{-1} for the uncatalyzed reference reaction in aqueous solution.

For the calibration of the activation free energy of the reference reaction in aqueous solution, we used a rate constant k_1 of 7.5 × 10^{-9} M^{-1} s^{-1} that was observed for the hydrolysis of cTMP by hydroxide ion.[34] Here we assumed that the hydrolysis of cAMP by hydroxide has the same rate constant. After inserting this rate constant and the corresponding pK_a for H_2O (15.5) in the Brønsted linear free energy relationship (LFER)

$$\log\left(\frac{k_1}{k_2}\right) = \beta_{nuc}[pK_a(1) - pK_a(2)] \quad (10)$$

with a slope (β_{nuc}) of 0.30,[35] we estimated the rate constant for the case in which the attacking nucleophile is PP_i [$pK_a(PP_i)$ = 8.9[36]] as k_2 = 7.8 × 10^{-11} M^{-1} s^{-1}. This rate constant can be converted using the transition state theory[37]

$$k_{TST} = \frac{k_B T}{h} \exp\left(-\frac{\Delta g^{\ddagger}}{k_B T}\right) \quad (11)$$

where k_B and h are Boltzmann's and Planck's constants, respectively, to an activation free energy $\Delta g^{\ddagger}$ of 31.4 kcal mol^{-1} at 300 K. An additional 2.4 kcal mol^{-1} barrier reduction due to the "cage" effect[20] was also used to account for the intramolecular character of our reference reaction. The resulting 29.0 kcal mol^{-1} activation free energy for the backward reference reaction translates to the activation free energy of 33.0 kcal mol^{-1} for the ATP → cAMP + PP_i reaction in aqueous solution at pH 7 (Figure 5). This activation barrier applies to the extrinsic mechanism and includes the nucleophile deprotonation free energy at pH 7.

For the general base mechanism, we assumed that the PT from the nucleophile is completed prior to the nucleophilic attack step. Then, because the free energy required to activate the nucleophile by the transfer of its proton to histidine is 1.3 kcal mol^{-1} larger than for the extrinsic mechanism, the overall barrier becomes 34.3 kcal mol^{-1} for the general base mechanism (Figure 6). Finally, the reaction free energy of 5.3 kcal mol^{-1} is shown in Figure 6 as the free energy of state IVg is 1.3 kcal mol^{-1} larger than that of state IVe (Figure 5) because the IVg → IVe histidine deprotonation step is not examined by our EVB calculations.

In addition to supporting our EVB calibration for adenylyl cyclases by sound estimates of the activation and reaction free

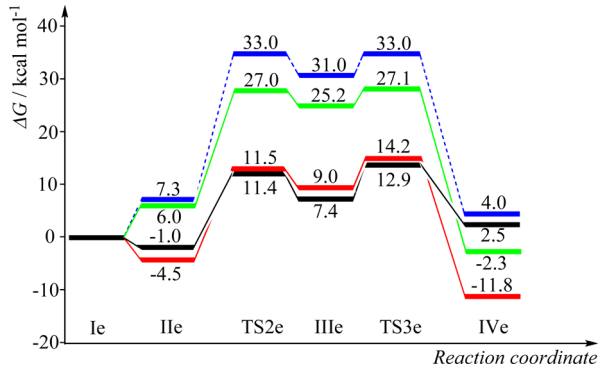

Figure 5. Calculated relative free energies for the extrinsic mechanism. Valence bond states involved in this mechanism are shown in Figure 4. The catalytic reactions of WT EF-ACD and its K346R mutant calculated using simulations initiated from the 1XFV enzyme structure are colored black and red, respectively. The free energy profile from simulations of the catalytic reaction of WT EF-ACD initiated from the 1SK6 structure is colored green. The energetics of the corresponding reference reaction in aqueous solution is colored blue.

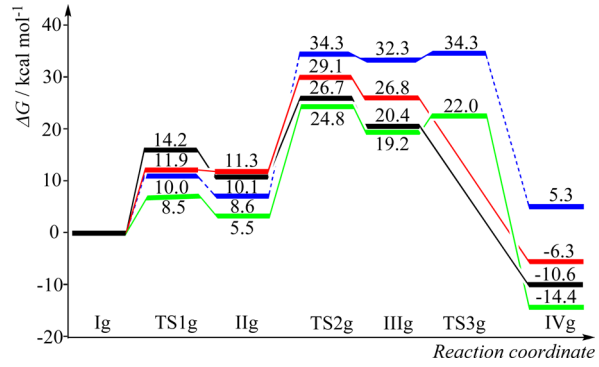

Figure 6. Calculated relative free energies for the general base mechanism. Valence bond states involved in this mechanism are shown in Figure 4. The catalytic reactions of WT EF-ACD and its K346R mutant calculated using simulations initiated from the 1XFV enzyme structure are colored black and red, respectively. The free energy profile from simulations of the catalytic reaction of WT EF-ACD initiated from the 1SK6 structure is colored green. The energetics of the corresponding reference reaction in aqueous solution is colored blue.

energies for the uncatalyzed reaction in aqueous solution, we needed to establish a realistic free energy profile for this reaction. In accordance with the shape of the two-dimensional ab initio quantum surface for the methanolysis of methyl phosphate in 1 M OH^-,[38] we placed the barriers for the nucleophilic attack and departure of the leaving group from the dianionic phosphorane intermediate at an equal height on a nearly flat free energy surface (blue profiles in Figures 5 and 6). Replacing the methanol leaving group in methyl phosphate with a better leaving group (PP_i) in ATP would likely result in the disappearance of the shallow minimum for the pentavalent phosphorane intermediate, thus yielding a fully concerted reaction. We retained the stepwise character of the reaction because this mechanism can be more efficiently implemented in the framework of the EVB methodology. This is because significantly longer simulations are required to properly sample the concerted process, in part because of difficulties with the implementation of the energy gap reaction coordinate for concerted pathways. Because partial atomic charges in the

dx.doi.org/10.1021/bi400088y | Biochemistry 2013, 52, 2672−2682

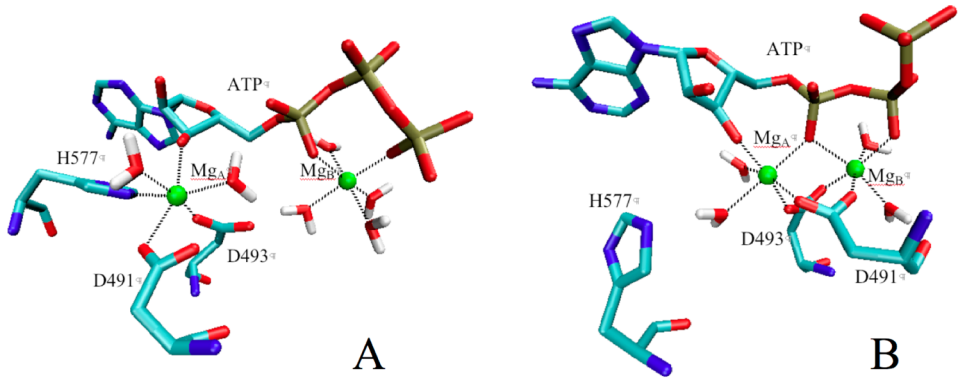

Figure 7. Metal coordination in the intermediate formed by deprotonating the O3′ nucleophile (state II in Figure 5). The metal coordination and the substrate and active site residue conformations vary depending on whether the computer simulations were started from the crystal structure of EF with bound dATP (A) or with bound cAMP and PP_i (B). Hydrogen atoms on the protein and substrate are not shown.

Table 1. Comparison of the Calculated[a] and Observed[11] Rate Constants and Activation Free Energies for the WT and K346R Mutant of EF-ACD

enzyme	ΔG_{PT} (kcal mol^{-1})	K	$\Delta g^{\ddagger}$ (kcal mol^{-1})	k (s^{-1})	k_{cat}^{calc} (s^{-1})	k_{cat}^{exp} (s^{-1})	Δg_{cat}^{calc} (kcal mol^{-1})	Δg_{cat}^{exp} (kcal mol^{-1})
WT	−1.0	5.4	13.9	467.8	394.1	1200	14.0	13.3
mutant	−4.5	1897	18.7	0.1490	0.1489	0.005	18.7	20.7

[a]To compare the calculated free energy profile with the observed steady state kinetics, we used the kinetic scheme $E + S \overset{K_s}{\rightleftharpoons} ES \overset{K}{\rightleftharpoons} ES' \overset{k}{\rightarrow} E + P$, where K_s is the dissociation constant for dissociation of the enzyme−substrate complex (ES) to E and S [$K_s = ([E][S])/[ES]$], K is the equilibrium constant ($K = [ES']/[ES]$) between ES with protonated ATP and its deprotonated form (ES′), and k is the rate constant for the rate-limiting step whose free energy $\Delta g^{\ddagger}$ is determined by the highest point on the calculated free energy profile and the plateau after the proton transfer step (state II/ex). Here we used the fact that the calculated reaction intermediate (III/ex in Figure 5) is so unstable that its existence does not affect the observed kinetics. The constants k and K were determined using the transition state theory (eq 11) and the relationship between the equilibrium constant and free energy difference, $\Delta G_{PT} = -RT \ln K$. The steady state catalytic constant, k_{cat}, was calculated as $k_{cat} = (kK)/(1 + K)$.[46]

phosphorane transition state and intermediate are similar and the overall surface retains its high-energy plateau character in both scenarios, the amount of stabilization by the protein environment should also be similar for the concerted and stepwise mechanisms that proceed via structurally similar pentavalent states. Thus, our stepwise model for the uncatalyzed reaction should be able to adequately capture the catalytic effects of adenylyl cyclases.

Enzyme-Catalyzed Reaction. The calculated free energy profiles for the uncatalyzed and enzyme-catalyzed reactions are presented for either the extrinsic or the general base mechanism in Figures 5 and 6, respectively. For each mechanism (Figure 2), separate free energy profiles are presented for two different initial substrate conformations and positions of the two Mg^{2+} ions. These disparate initial geometries, which cannot be sampled in a single MD simulation,[18] were based on X-ray diffraction data obtained from crystals that were grown under different conditions.[16,17]

The overall energetics for the activation of the 3′-O nucleophile (O_{nuc}) and the subsequent associative PO bond formation and cleavage (Figure 2) are more favorable when the nucleophile activation occurs via the extrinsic rather than the general base mechanism (cf. Figures 5 and 6). This is because the rate-limiting activation barrier of 12.9 kcal mol^{-1} for the extrinsic mechanism simulated from the EF-ATP complex[17] (PDB entry 1XFV) is significantly lower than the value of 24.8 kcal mol^{-1} calculated for the general base mechanism. The general base mechanism becomes more favorable than the extrinsic one only for calculations that were started from the crystal structure of the EF−cAMP complex (27.1 and 24.8 kcal mol^{-1} for the extrinsic and general base mechanisms, respectively)[16] (PDB entry 1SK6). Therefore, our description of the calculated results, their discussion, and comparison with experimental kinetics (Table 1) will focus on the extrinsic mechanism.

The K346R mutant was also calculated to favor the extrinsic mechanism. The deprotonated nucleophile (Figure 5, state II) is predicted to be more stable than its neutral form (Figure 5, state I) in both the mutant and WT. This stabilization is due to direct coordination of the Mg_A ion to the O3′$^-$ atom of the ribose (Figure 7A). In contrast, a significant destabilization of the deprotonated nucleophile [$\Delta G = 6.0$ kcal mol^{-1} (Figure 5)] was obtained in simulations initiated from the crystal structure of the product. This destabilization can be attributed to the repulsive interaction between O3′$^-$ and one of the anionic oxygen atoms of the α-phosphate (Figure 7B). Because of a longer O3′−phosphate distance, which can be attributed to differences in Mg_A coordination (cf. panels A and B of Figure 7), this destabilizing electrostatic interaction is weaker in the simulations initiated from the 1XFV crystal structure (Figure 7A). Thus, the calculated energetic differences can be traced back to significantly different conformational states of ATP in the two crystal structures.

Because Arg 346 H-bonds with the deprotonated O3′ atom (O3′−N distance of 2.8 Å) but Lys 346 does not, the relative free energy of the deprotonated intermediate in the extrinsic mechanism (Figure 5, state II) improves from −1.0 to −4.5 kcal mol^{-1} in the K346R mutant. The new H-bonds from Arg 346 to O3′ and α-phosphate are formed along the forward deprotonation trajectory, while the initial close contact of Arg 346 with the γ-phosphate disappears. This deprotonation-induced structural reorganization of the mutant could be a useful structural marker for the assignment of the protonation state of the ribose in the crystal structure of the K346R mutant.

dx.doi.org/10.1021/bi400088y | Biochemistry 2013, 52, 2672−2682

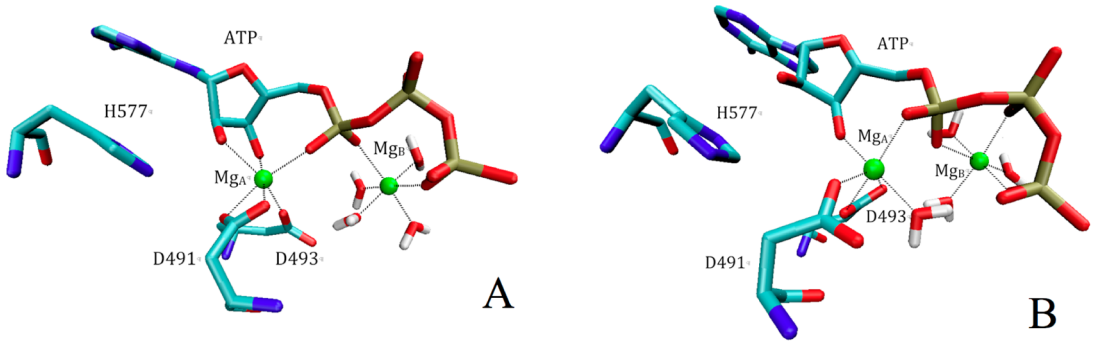

Figure 8. Metal coordination to assist the nucleophilic attack step of the reaction for the WT (A) and mutant EF-ACD (B). Hydrogen atoms on the protein and substrate are not shown.

In addition, the structural integrity of our calculations could be verified by cocrystallizing the K346R mutant with an unreactive ATP analogue, for example, the one with the $\alpha-\beta$ bridging oxygen substituted by the NH or CH_2 group, which would allow us to observe the predicted Arg 346−O3′ interaction.

A notable reorganization of the metal−ligand interactions was observed during the attack of O3′ on P_α in the simulations of both the WT (cf. Figures 7A and 8A) and the K346R mutant (Figure 8B). After this reorganization, oxygen atoms of the α-phosphate and O2′H groups became directly coordinated to Mg_A. The direct coordination of the anionic oxygen atoms on α-phosphate by both metal ions was retained in the transition states for the nucleophilic attack (Figure 5, state TS2) and the departure of the leaving group (Figure 5, state TS3), and in the pentavalent intermediate (Figure 5, state III).

The ability of our calculations to reveal the reaction coordinate contribution by the coordinates other than $P_\alpha-O$ bond distances is facilitated by our use of the λ-dependent collective reaction coordinate that specifies the initial and final EVB states but not the geometric details of their connecting pathway. However, this rigorous approach to discovering important mechanistic contributions appear to be more sensitive to the MD sampling of the configurational space than the simple geometric reaction coordinate employed by non-EVB QM/MM studies.

To address this methodological aspect of our calculations we evaluated the hysteresis of the calculated free energy profile by running λ-based sampling (eq 3) for a given reaction step first in the forward and then in the reverse direction (Tables 3S and 4S of the Supporting Information). In some cases, we followed these two simulations by a second forward calculation that was started from the end point of the reverse simulation. The energies sampled in the last two calculations (i.e., forward and reverse or reverse and forward) were also analyzed using the pooled sampling approach of eq 8 (Tables 3S and 4S of the Supporting Information).

The comparison of the reaction free energies for the forward $[\Delta G(f)]$ and reverse $[\Delta G(r)]$ trajectories shows that the initial state is afforded extra stabilization: for example, $\Delta G_{IIIe\rightarrow IVe}(f)$ and $\Delta G_{IIIe\rightarrow IVe}(r)$ equal −9.6 and −32.5 kcal mol^{-1}, respectively, in the K346R mutant (Table 3S of the Supporting Information). In most cases, for example, $\Delta G_{IIIe\rightarrow IVe}(f)$ and $\Delta G_{IIIe\rightarrow IVe}(r)$ reaction steps in the WT, this trend is almost completely compensated by the hysteresis of the same reaction step in water, which also favors the initial state. Overall, the calculated hysteresis significantly decreases when the forward trajectory is calculated for the second time from the end point of the reverse trajectory simulation $[\Delta G(f_2)]$. For example, $\Delta G_{IIe\rightarrow IIIe}(f)$, $\Delta G_{IIe\rightarrow IIIe}(r)$, and $\Delta G_{IIe\rightarrow IIIe}(f_2)$ values in the K346 mutant amount to 40.1, 13.3, and 17.2 kcal mol^{-1}, respectively.

Because the extra stabilization of the free energy of the initial state is approximately the same in the forward and reverse directions, it is possible to significantly increase the accuracy of the calculated free energies by simple arithmetic averaging of $\Delta G(f)$ and $\Delta G(r)$ values for the same reaction step. Alternatively, and more rigorously, the EVB accuracy can be improved by calculating free energies from the joint forward and reverse energy pool as described in eq 8. For the reactions examined in Table 3S of the Supporting Information, these pooled free energies differ from simple averaging by less than 1 kcal mol^{-1} for ΔG and less than 2 kcal mol^{-1} for $\Delta g^{\ddagger}$.

The stabilization of states TS2, TS3, and III by the enzyme environment is larger in the WT than in the K346R mutant (Figure 5), but the energetic differences of ∼1 kcal mol^{-1} are too small to be attributable to a single dominant interaction. The comparison of average geometries of the rate-limiting transition state (TS3) in the WT and mutant enzymes is shown in Figure 9. Considering the calculated $P-O_{nuc}$ and $P-O_{lg}$ distances of 1.6 and 2.3 Å, respectively, this TS occurs late on the PO bond making and breaking reaction coordinate. The $P-O_{lg}$ distances in this TS become longer by an additional 0.16 Å in the mutant enzyme. The redistribution of the negative charge toward the nonbridging oxygen atoms of α-phosphate and O_{lg}

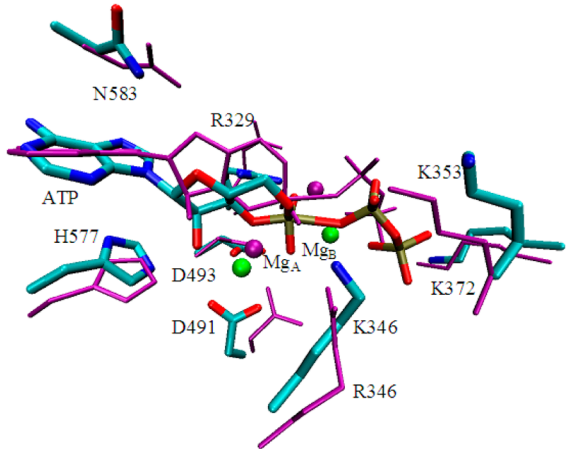

Figure 9. Superposition of the average TS3 geometries for the extrinsic mechanism in the WT (atom-type colors) and K346R mutant (purple color) of EF-ACD. Hydrogen atoms and water molecules are not shown.

dx.doi.org/10.1021/bi400088y | *Biochemistry* 2013, 52, 2672−2682

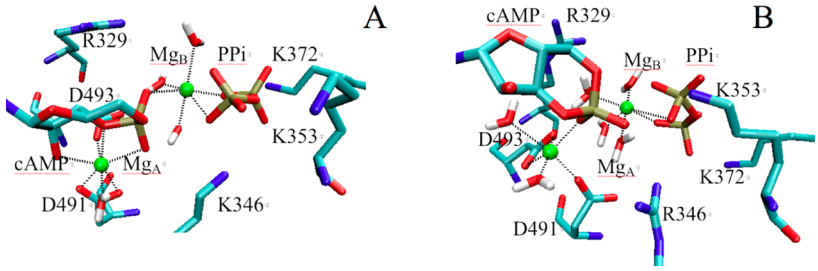

Figure 10. Metal coordination in the product state of the reaction catalyzed by WT (A) and mutant EF-ACD (B). Hydrogen atoms on the protein, cAMP, and PP_i molecules are not shown.

in this high-energy configuration of the substrate is stabilized by interactions with surrounding positively charged lysine side chains. In particular, Lys 346 forms a 3.1 Å H-bond with O_{lg} that is partly lost in the mutant. However, this loss is compensated in the mutant by shorter distances from the negative oxygen atoms of the substrate to Lys 353 and Lys 372.

The structural and energetic effect of the arginine at position 346 of the mutant enzyme is the most pronounced in the product state of the reaction (IVe), as this residue allows pyrophosphate (PP_i) in the K346R mutant to drift to a distance (4.3 Å from P of cAMP to the closest oxygen on PP_i) that is longer than that of the WT enzyme (3.3 Å) (Figure 10). The increased separation of the two negatively charged products in the mutant enzyme is associated with a reorganization of the first coordination sphere of Mg_B, which contains four water molecules and two oxygen atoms on PP_i but no atoms of cAMP. The free energy of the product state in the mutant is thus significantly lowered by weaker electrostatic repulsion between phosphate groups of cAMP and PP_i.

DISCUSSION

We have studied the two-metal ion catalysis of anthrax edema factor using a combination of FEP–MD and US–EVB methods. The advantage of our computer simulation protocol resides in the cancellation of systematic errors in the intrinsic quantum mechanical bond energies. This cancellation can occur because energies of equivalent bonds are postulated to be the same in the enzyme active site and in aqueous solution. This advantage allows us to focus on the catalytically important differential solvation effects of the water and enzyme environments that can be related to the k_{cat}/k_{wat} ratio.[39,40] Inspecting relative free energies in two protein variants, WT EF-ACD and its K346R mutant, and protein environments from two different crystal structures further leverages this strength of our approach.

We chose to study two mechanistic options that differed in the mechanism of nucleophile activation but shared a pentavalent phosphorane dianion as a high-energy intermediate. Although this species appears to be a transition state rather than intermediate in the uncatalyzed reaction,[38,41] the construction of this intermediate as a distinct valence bond state allowed us to drive the MD simulation over the barrier while extensively sampling relevant atomic charges and geometries near this barrier. The two-state concerted pathway, in which the system would be driven from state II directly to state IV, was not examined because the construction of the mapping potential from these two diabatic states (eq 3) would not allow the anionic nonbridging oxygen atoms on the α-phosphate to become more negative in the TS than in state II or IV. This charge shift is an important feature of phosphate diester hydrolysis.[38] Additionally, the sampled energy differences of diabatic states II and IV that define the E_{gap} reaction coordinate (eq 7) for the concerted reaction tend to significantly fluctuate near the reactant and product structures. These E_{gap} fluctuations obstruct the location of the reactant and product minima on the free energy curve. Although this difficulty can be in principle compensated by more extensive sampling and perhaps by a clever force field design, we did not feel that it would provide any advantage over our quasi-concerted pathway that passes via a high-energy state III. At any rate, the free energy surface appears to be sufficiently deformed in the enzyme for the phosphorane to represent the true intermediate in the enzyme-catalyzed reaction (Figure 5).

Our general understanding and acceptance of EVB applications in enzymology would benefit from a deeper methodological analysis of this method. Therefore, in addition to providing extensive information about the parameters of the diabatic states (Tables 5S–16S of the Supporting Information), we examined the effects and advantages of the pooled sampling from independent forward and reverse trajectories. This procedure was designed to better include contributions of the exchange of metal ligands and conformational changes of the side chains in the active site to the calculated reaction and activation free energies. These structural effects can be essential for enzyme catalysis; for example, a conformational change in the P-loop of ras GTPase was found to significantly promote catalysis by this enzyme.[42] Because the simulation of the reaction path is too short for the huge size of the phase space and we are not able to control the sampling along the E_{gap} coordinate (eq 7) in the conventional EVB/FEP–US method, it takes several independent forward and reverse simulations to sample catalytically significant configurational space. Although for our reaction the use of a simple average of the forward and reverse free energy profiles provided results similar to those of pooled sampling, this may not be true for every reaction. Because the weight of the two profiles is equivalent in the average profile, it can happen that one of the profiles has a significantly higher energetics (because of the unfavorable geometry), so its contribution to the overall free energy may be overestimated. With the pooled sampling, the irrelevant geometries automatically have a small weight. Alternatively, a technique that allows the precise control of the E_{gap} reaction coordinate exists,[43] but this method requires the knowledge of the completely parametrized EVB ground state energy surface. In this work, our plan was to increase the extent of sampling using the conventional EVB strategy and not the precise driving of the system on the EVB surface. The pooled sampling approach seems to accomplish this goal.

The two-metal ion active site model of EF-ACD that contained a conformation of the ATP substrate observed in the

dx.doi.org/10.1021/bi400088y | Biochemistry 2013, 52, 2672–2682

1XFV crystal showed significant catalysis, which did not require participation of His 351 as a general base. The catalytic rate constants of 394.1 and 0.1489 s^{-1} calculated for the WT and K346 mutant, respectively, agree reasonably well with their experimental counterparts of 1.2 × 10^3 and 0.005 s^{-1}, respectively[11] (Table 1). The agreement with the experiment further improves when our k_{cat} for WT is compared with a k_{cat} of 680 ± 270 s^{-1} that was obtained using a different biochemical assay.[44] Previously, we showed that the ATP binding free energy (−6 kcal mol^{-1}) for binding to the two-metal ion active site of EF-ACD agrees reasonably well with the corresponding experimental value.[17] Because all the reaction and activation free energies were calculated without introducing any adjustable parameters for the simulations in the protein environment, the two-metal active site observed in the crystal structure of the EF−CaM−3′-dATP complex (PDB entry 1XFV)[17] represents a viable structural representation of the ground state of the EF-catalyzed reaction.

We did not examine the transfer of a proton from the 3′-OH nucleophile to one of the α-phosphate nonbridging oxygen atoms because such a mechanism is associated with a very high activation barrier in a related nucleotidyl transfer reaction.[14] Although this substrate-assisted mechanism is popular for enzymatic GTP and phosphate monoester hydrolysis reactions,[45] it incurs an extra energetic penalty for diester-like substrates because of the significantly lower basicity of the α-phosphate compared to that of the γ-phosphate. Similarly, the small k_{cat} effect of the His351Lys point mutation in EF-ACD,[17] and our earlier experience with the comparison of the one- and two-metal mechanisms in BamHI restriction endonuclease,[15] pointed to the two-metal mechanism as the most likely mechanism utilized by EF-ACD. Perhaps more importantly, we did not explicitly consider the single-metal ion catalysis in this study because of large computational difficulties associated with the accurate evaluation of the energetics of the reference reaction in the absence of the structural Mg^{2+} ion (Mg_B^{2+}) that balances large negative charges on the triphosphate chain. Thus, it is still possible that the enzyme might be versatile enough to catalyze cAMP formation using both two-metal and single-metal, general base pathways. Evolutional selection of such a broader mechanistic arsenal could allow the bacteria to overcome various cell defenses.

■ ASSOCIATED CONTENT

Ⓢ Supporting Information

Additional details regarding the EVB force field parameters (Figure 1S and Tables 5S−16S), structural properties of models at the reactant state (Figure 2S and Tables 1S and 2S), and energetics of individual and commonly sampled reaction steps (Tables 3S and 4S). This material is available free of charge via the Internet at http://pubs.acs.org.

■ AUTHOR INFORMATION

Corresponding Author

*E-mail: jfloria@luc.edu. Phone: (773) 508-3785.

Present Address

[§]L.M.: University of Cambridge, Cambridge, United Kingdom.

Funding

This work was supported by National Institutes of Health Grant GM62548.

Notes

The authors declare no competing financial interest.

■ ABBREVIATIONS

cAMP, cyclic AMP; EF, edema factor; ACD, adenylyl cyclase domain; CAM, calmodulin; PP_i, pyrophosphate; FEP, free energy perturbation; EVB, empirical valence bond; LRF, local reaction field; MD, molecular dynamics; TS, transition state; WT, wild type.

■ REFERENCES

(1) Sutherland, E. W. (1970) On the Biological Role of Cyclic AMP. *J. Am. Med. Assoc. 214*, 1281−1288.

(2) Bourne, H. R., Weinstein, Y., Melmon, K. L., Lichtenstein, L. M., Henney, C. S., and Shearer, G. M. (1974) Modulation of inflammation and immunity by cyclic AMP. *Science 184*, 19−28.

(3) Kawasaki, H., Springett, G. M., Mochizuki, N., Toki, S., Nakaya, M., Matsuda, M., Housman, D. E., and Graybiel, A. M. (1998) A Family of cAMP-Binding Proteins That Directly Activate Rap1. *Science 282*, 2275−2279.

(4) Leppla, S. H. (1982) Anthrax toxin edema factor: A bacterial adenylate cyclase that increases cyclic AMP concentrations of eukaryotic cells. *Proc. Natl. Acad. Sci. U.S.A. 79*, 3162−3166.

(5) Tang, W.-J., and Guo, Q. (2009) The adenylyl cyclase activity of anthrax edema factor. *Mol. Aspects Med. 30*, 423−430.

(6) Ladant, D., and Ullmann, A. (1999) *Bordatella pertussis* adenylate cyclase: A toxin with multiple talents. *Trends Microbiol. 7*, 172−176.

(7) Young, J. A., and Collier, R. J. (2007) Anthrax toxin: Receptor binding, internalization, pore formation, and translocation. *Annu. Rev. Biochem. 76*, 243−265.

(8) Kim, C., Wilcox-Adelman, S., Sano, Y., Tang, W.-J., Collier, R. J., and Park, J. M. (2008) Antiinflammatory cAMP signaling and cell migration genes co-opted by the anthrax bacillus. *Proc. Natl. Acad. Sci. U.S.A. 105*, 6150−6155.

(9) Dumetz, F., Jouvion, G., Khun, H., Glomski, I. J., Corre, J.-P., Rougeaux, C., Tang, W.-J., Mock, M., Huerre, M., and Goossens, P. L. (2011) Noninvasive imaging technologies reveal edema toxin as a key virulence factor in anthrax. *Am. J. Pathol. 178*, 2523−2535.

(10) Tesmer, J., Sunahara, S., Johnson, R., Gosselin, G., Gilman, A., and Sprang, S. R. (1999) Two-metal-ion catalysis in adenylyl cyclase. *Science 285*, 756−760.

(11) Drum, C. L., Yan, S.-Z., Bard, J., Shen, Y.-Q., Lu, D., Soelaiman, S., Grabarek, Z., Bohm, A., and Tang, W. J. (2002) Structural basis for the activation of anthrax adenylyl cyclase exotoxin by calmodulin. *Nature 415*, 396−402.

(12) Mou, T.-C., Masada, N., Cooper, D. M. F., and Sprang, S. R. (2009) Structural Basis for Inhibition of Mammalian Adenylyl Cyclase by Calcium. *Biochemistry 48*, 3387−3397.

(13) Steitz, T. A., and Steitz, J. A. (1993) A General Two-metal-ion Mechanism for Catalytic RNA. *Proc. Natl. Acad. Sci. U.S.A. 90*, 6498−6502.

(14) Florián, J., Goodman, M. F., and Warshel, A. (2003) Computer simulation of the chemical catalysis of DNA polymerases: Discriminating between alternative nucleotide insertion mechanisms for T7 DNA polymerase. *J. Am. Chem. Soc. 125*, 8163−8177.

(15) Mones, L., Kulhanek, P., Florián, J., Simon, I., and Fuxreiter, M. (2007) Probing the Two-Metal Ion Mechanism in the Restriction Endonuclease BamHI. *Biochemistry 46*, 14514−14523.

(16) Guo, Q., Shen, Y., Zhukovskaya, N. L., Florián, J., and Tang, W. J. (2004) Structural and kinetic analyses of the interaction of anthrax adenylyl cyclase toxin with reaction products cAMP and pyrophosphate. *J. Biol. Chem. 279*, 29427−29435.

(17) Shen, Y., Zhukovskaya, N. L., Guo, Q., Florián, J., and Tang, W. J. (2005) Calcium-independent calmodulin binding and two-metal-ion catalytic mechanism of anthrax edema factor. *EMBO J. 24*, 929−941.

(18) Martinez, L., Laine, E., Malliavin, T., Nilges, M., and Blondel, A. (2009) ATP Conformations and Ion Binding Modes in the Active Site of Anthrax Edema Factor: A Computational Analysis. *Proteins 77*, 971−983.

(19) Warshel, A., and Weiss, R. M. (1980) An Empirical Valence Bond Approach for Comparing Reactions in Solutions and in Enzymes. *J. Am. Chem. Soc. 102*, 6218−6226.
(20) Warshel, A. (1991) *Computer Modeling of Chemical Reactions in Enzymes and Solutions*, Wiley, New York.
(21) Zwanzig, R. W. (1954) High-Temperature Equation of State by a Perturbation Method. I. Nonpolar Gases. *J. Chem. Phys. 22*, 1420−1426.
(22) Case, D. A., Darden, T., Cheatham, T. E., III, Simmerling, C. L., Wang, J., Duke, R. E., Luo, R., Merz, K. M., Pearlman, D. A., Crowley, M., Walker, R. C., Zhang, W., Wang, B., Hayik, S., Roitberg, A., Seabra, G., Wong, K. F., Paesani, F., Wu, X., Brozell, S., Tsui, V., Gohlke, H., Yang, L., Tan, C., Mongan, J., Hornak, V., Cui, G., Beroza, P., Matthews, D. H., Schafmeister, C., Ross, W. S., and Kollman, P. A. (2006) *Amber 9*, University of California, San Francisco.
(23) Bren, U., Martinek, V., and Florián, J. (2006) Decomposition of the solvation free energy of deoxyribonucleoside triphosphates using the free energy perturbation method. *J. Phys. Chem. B 110*, 12782−12788.
(24) Bren, U., Martinek, V., and Florián, J. (2006) Free Energy Simulations of Uncatalyzed DNA Replication Fidelity: Structure and Stability of T-G and dTTP-G Terminal DNA Mismatches Flanked by a Single Dangling Nucleotide. *J. Phys. Chem. B 110*, 10557−10566.
(25) Sucato, C. A., Upton, T. G., Kashemirov, B. A., Martínek, V., Xiang, Y., Beard, W. A., Batra, V. K., Pedersen, L. C., Wilson, S. H., McKenna, C. E., Florián, J., Warshel, A., and Goodman, M. F. (2007) Modifying the β-γ leaving-group bridging oxygen alters nucleotide incorporation efficiency, fidelity and catalytic mechanism of DNA polymerase β. *Biochemistry 46*, 461−471.
(26) Klvana, M., Jerábek, P., Goodman, M. F., and Florián, J. (2011) An Abridged Transition State Model To Derive Structure, Dynamics, and Energy Components of DNA Polymerase β Fidelity. *Biochemistry 50*, 7023−7032.
(27) Cornell, W. D., Cieplak, P., Bayly, C. I., Gould, I. R., Merz, K. M., Jr., Ferguson, D. M., Spellmeyer, D. C., Fox, T., Caldwell, J. W., and Kollman, P. A. (1995) A second generation force field for the simulation of proteins, nucleic acids, and organic molecules. *J. Am. Chem. Soc. 117*, 5179−5197.
(28) Marelius, J., Kolmodin, K., Feierberg, I., and Åqvist, J. (1999) Q: A molecular dynamics program for free energy calculations and empirical valence bond simulations in biomolecular systems. *J. Mol. Graphics Modell. 16*, 213−225.
(29) Ryckaert, J.-P., Ciccotti, G., and Berendsen, H. J. C. (1977) Numerical Integration of the Cartesian Equations of Motion of a System with Constraints: Molecular Dynamics of n-Alkanes. *J. Comput. Phys. 23*, 327−341.
(30) Lee, F. S., and Warshel, A. (1992) A local reaction field method for fast evaluation of long-range electrostatic interactions in molecular simulations. *J. Chem. Phys. 97*, 3100−3107.
(31) Izatt, R. M., Rytting, J. H., Hansen, L. D., and Christensen, J. J. (1966) Thermodynamics of Proton Dissociation in Dilute Aqueous Solution. V. An Entropy Titration Study of Adenosine, Pentoses, Hexoses, and Related Compound. *J. Am. Chem. Soc. 88*, 2641−2645.
(32) Eigen, M., and de Mayer, L. (1955) Kinetics of neutralization. *Electrochemistry 59*, 986−993.
(33) Hayaishi, O., Greengard, P., and Colowick, S. P. (1971) On the Equilibrium of the Adenylate Cyclase Reaction. *J. Biol. Chem. 246*, 5840−5843.
(34) Gerlt, J. A., Westheimer, F. H., and Sturtevant, J. M. (1975) The enthalpies of hydrolysis of acyclic, monocyclic, and glycoside cyclic phosphate diesters. *J. Biol. Chem. 250*, 5059−5067.
(35) Kirby, A. J., Manfredi, A. M., Souza, B. S., Medeiros, M., Priebe, J. P., Brandão, T. A. S., and Nome, F. (2008) Reactions of α-nucleophiles with a model phosphate diester. *ARKIVOC (Gainesville, FL, U.S.) 2009*, 28−38.
(36) Sucato, C. A., Upton, T. G., Kashemirov, B. A., Osuna, J., Oertell, K., Beard, W. A., Wilson, S. H., Florián, J., Warshel, A., McKenna, C. E., and Goodman, M. F. (2008) DNA Polymerase β Fidelity: Halomethylene-Modified Leaving Groups in Pre-Steady-State Kinetic Analysis Reveal Differences at the Chemical Transition State. *Biochemistry 47*, 870−879.
(37) Eyring, H. (1935) The activated complex and the absolute rate of chemical reactions. *Chem. Rev. 17*, 65−77.
(38) Borden, J., Crans, D., and Florián, J. (2006) Transition State Analogs for Nucleotidyl Transfer Reactions: Structure and Stability of Pentavalent Vanadate and Phosphate Ester Dianions. *J. Phys. Chem. B 110*, 14988−14999.
(39) Wolfenden, R., and Snider, R. J. (2001) The Depth of Chemical Time and the Power of Enzymes as Catalysts. *Acc. Chem. Res. 34*, 938−945.
(40) Warshel, A., and Florián, J. (1998) Computer simulations of enzyme catalysis: Finding out what has been optimized by evolution. *Proc. Natl. Acad. Sci. U.S.A. 95*, 5950−5955.
(41) Rosta, E., Kamerlin, S. C. L., and Warshel, A. (2008) On the interpretation of the observed linear free energy relationship in phosphate hydrolysis: A thorough computational study of phosphate diester hydrolysis in solution. *Biochemistry 47*, 3725−3735.
(42) Shurki, A., and Warshel, A. (2004) Why does the Ras switch "break" by oncogenic mutations? *Proteins: Struct., Funct., Bioinf. 55*, 1−10.
(43) Mones, L., Kulhánek, P., Simon, I., Laio, A., and Fuxreiter, M. (2009) The Energy Gap as a Universal Reaction Coordinate for the Simulation of Chemical Reactions. *J. Phys. Chem. B 113*, 7867−7873.
(44) Göttle, M., Dove, S., Kees, F., Schlossmann, J., Geduhn, J., König, B., Shen, Y., Tang, W.-J., Kaever, V., and Seifert, R. (2010) Cytidylyl and Uridylyl Cyclase Activity of *Bacillus anthracis* Edema Factor and *Bordetella pertussis* CyaA. *Biochemistry 49*, 5494−5503.
(45) Kamerlin, S. C. L., Prasad, B. R., Sharma, P. K., and Warshel, A. (2013) Why Nature Really Choose Phosphate? *Q. Rev. Biophys. 46*, 1−132.
(46) Fersht, A. R. (1999) *Structure and Mechanism in Protein Science*, W. H. Freeman and Co., New York.